Numerical investigation of the irreversible behavior of GDL under cyclic hygrothermal loading

Fabien Mons-Quendo, Jean-François Blachot, Jean-Philippe Poirot-Crouvezier, Sebastien Kawka, Christophe Carral, Patrice Mele

Numerical investigation of the irreversible behavior of GDL under cyclic hygrothermal loading

Fabien MONS-QUENDO[1], Jean-François BLACHOT[1,z], Jean-Philippe POIROT-CROUVEZIER[1], Sébastien KAWKA[1], Christophe CARRAL[2], Patrice MELE[2]

[1]Univ. Grenoble Alpes, CEA, Liten DEHT, 38000 Grenoble, France

[2]Univ. Grenoble Alpes, Univ. Savoie Mont Blanc, CNRS, Grenoble INP, LEPMI, 38000 Grenoble, France

[z]Corresponding author: jean-françois.blachot@cea.fr

Abstract

Performances of Proton Exchange Membrane Fuel Cells (PEMFC) are impacted by the physical properties of the Gas Diffusion Layer (GDL). These properties, such as thickness or porosity, are modified irreversibly by diverse processes, notably by the clamping of the PEMFC or the swelling of the membrane during cell operation, which can lead to irreversible deformation. This phenomenon difficult to apprehend experimentally, is also challenging to be investigated numerically. An elastoplastic law related to the irreversible strain of the GDL after compression is proposed in this study and implemented in a Finite Element Model (FEM). Variations in GDL's properties during humidity and temperature cycles are studied depending on PEMFC clamping methods, using experiments and numerical simulations. The influences of processing conditions, i.e. the Membrane Electrode Assembly (MEA) hot pressing process, on GDLs properties are also studied. Numerical results show the importance to take into account the evolution of the mechanical properties of PEMFC components. In particular, the irreversible strain of the GDL during cell operation is a crucial parameter to increase the performance and durability of PEMFCs.

1. Introduction

Interest in proton exchange membrane fuel cells has grown significantly in recent decades. PEMFCs are promising energy conversion devices for stationary and transportation applications [1]. However, improvements of their durability and of their performances are still needed to become competitive with combustion engines. For 2025, the U.S Department of Energy has set a durability target of 8,000 hours, which corresponds to 150,000 miles of driving [2].

Mechanical behavior of PEMFC and its components affects the overall performance and durability of the device [3,4]. The clamping of the stack generates mechanical stresses that need to be controlled. Low compression leads to high interfacial resistance. Conversely, excessive compression reduces diffusivity and increases the intrusion of the Gas Diffusion Layer (GDL) inside the channels [5], leading to increased pressure losses in the channels, thus reducing the total efficiency. The clamping of the stack is then a balance between bulk electrical resistance and gas transport properties [6–8]. Moreover, during stack operation, PEMFCs are subjected to different sources of mechanical stresses due to vibration, freeze/thaw cycles or hygrothermal cycles [9,10].

Among all the components of the fuel cell, the GDL is the most sensitive to compressive stresses, which lead to its permanent damage [11–16]. In fact, GDL is a critical material whose functions are to transport reactants from the channel to the catalyst layer, to ensure electrical contact with the bipolar plate (BPP), and to give the proper mechanical support for the components of the Membrane Electrode Assembly (MEA). Understanding its mechanical behavior is a key point for improving the durability and the performance of MEAs and hence PEMFCs [17,18].

Numerous studies have been carried out in the literature to gain a better understanding of the influence of the stack clamping on the mechanics of the various PEMFC components [7,8,19–24]. Some of them have modeled the stress level generated during cell operation [25–29]. However, the modelled material properties, geometries, or even scale, differ from one study to another, inhibiting comparisons.

Modelling the mechanical behavior of a fibrous material as GDLs is complex because of its non-linear anisotropic mechanical behavior [30]. Nevertheless, the published models presented below considered GDLs as a homogeneous material. A recent study of Le Carre et al. [31] shows that this hypothesis cannot predict the complex behavior of the GDL under a land/channel pattern. The mechanical behavior of the GDL is defined as linear isotropic in numerous studies [3,28,32]. The results obtained with these models need to be regarded with caution as they tend to overestimate the porosity and the intrusion of the GDL inside the channel [21]. Kleemann et al. [22] proposed an orthotropic model with a fitting of Young's modulus measured during compression. Some studies used hyper-elastic model (Charbonné et al., 2021; Koorata and Bhat, 2021; Shen, 2017) and Koorata [33] carried out a comparison of several hyperelastic models to propose an advanced model taking into account the irreversible strain of the GDL and the hysteresis resulting from loading and unloading cycling. Because of the incompressible hypothesis associated to these hyperelastic models, the in-plane stress caused by the compression must be carefully considered, the out-of-plane Poisson's ratio being assumed to be null due to the high porosity of the material [22]. To overcome these limitations, some studies proposed a phenomenological model to explain the nonlinear behavior of the GDL [34–36].

Before the stack clamping, the membrane electrode assembly (MEA) is prepared by assembling the membrane with catalysts layers and GDLs on both sides. The catalyst layer can be supported by either the membrane or the GDL. However, the standard process involves hot pressing GDLs on the components. Thus, the GDLs are pre-compressed and their physical properties, like thickness, porosity and their mechanical properties are modified. The pressure applied during the hot pressing process depends on the components. [37,38]. The interfaces inside the MEA need to assure heat and charges conduction, and mass transport [39]. Mechanical adhesion between the components of the MEA is a fundamental aspect of the MEA interfaces. The delamination between the different layers is a common failure mode of the MEA, which inhibits local charge transfers, leading to a decrease in catalyst utilization [39]. Moreover, the delamination of the MEA can result in local water accumulation, leading to a decrease in mass transport [40]. Consequently, the simulation can help searchers to investigate the effects of hot pressing process on the components of the fuel cell and to adjust the process to different materials. Only few studies have focused on the mechanical impact of the hot pressing process. Koorata and Bhat [41] have proposed a phenomenological model of the GDL and have studied the effect of hot pressing pressure on the irrecoverable residual effect on the GDL. Their model shows that an increase

in the pressure applied during the hot press process induces an increase in GDL stiffness. However, their model is isotropic and the parameters required for their model are fit to a stress/strain curve until 1 MPa. These facts can lead to errors in the in-plane stress induced by the clamping process, or on the compressive stress under the land due to overstresses induced by the land/channel pattern. Ouerghemmi et al. [42] proposed a numerical study of the influence of the interfaces properties on the mechanical behavior of PEMFC showing a link between plastic deformation of the membrane and interfaces properties of the MEA's components. Ramani et al. [38] used simulation to highlight the favorable effect of a better adhesion between Catalyst Coated Membrane (CCM) and GDL.

In this study, an original numerical implementation of a semi-empirical law of the irreversible mechanical behavior of the GDL is proposed using an elastoplastic law. The impacts of the clamping process, hygrothermal loading and hot pressing process are then evaluated numerically via finite element simulations, and the results are discussed.

2. Material and methods

2.1 Geometry and boundaries conditions

Various fuel cell stack clampings are employed to ensure effective contact between components [15]. Two main types of clamping can be distinguished: those applying a constant force during the stack lifetime, and those maintaining a constant displacement. Therefore, we investigate both cases of the clamping process, called respectively "fixed pressure" (FP) and "fixed displacement" (FD), with an initial application of either force or displacement to the top edge of the BPP, during stack clamping. In this work, in order to compare both approaches, the initial value of pressure at the end of the stack clamping will be identical, whatever the type of clamping employed. The numerical simulation is performed with the finite element code COMSOL Multiphysics 6.2.

The geometry and boundaries conditions used for the numerical simulation are illustrated in Figure 1, which shows a half channel on the left side and a half land on the right side. It is made up of two parts of BPPs (stamped metal sheets, with the anode at the top and the cathode at the bottom), two GDLs and one membrane. As assumed in previous studies [23,25], particularities in the catalyst layer's mechanical behavior are neglected, and its thickness is taken into account in the gas diffusion layer. A pressure applied on the bipolar plates simulates the clamping. This pressure is determined to obtain 1 MPa on the active area. The different thicknesses of the materials are listed in Figure 1.

The simulations are done with generalized plane strain assumption.

The contact between the different layers of the membrane electrode assembly (MEA), consisting of the membrane, the anodic and cathodic catalyst layers and the two GDLs, is assumed to be bonded. Frictionless contacts are set at the GDLs/BPPs interfaces. A planar support is defined on the bottom and side edges of the cathode BPP part (Figure 1).

A Hygrothermal Stress Test (HST) is defined, adapted from Kusoglu's work [25], and consisting in a hygrothermal loading sequence representative of a fuel cell operation as used in the literature [27,28]. The complete sequence is shown in Figure 2, with five humidity cycles, associated to an initial increase of the temperature, followed by a stabilization and a final decrease. Before this sequence, the clamping of the stack is realized at a temperature (T) of

25°C, and a relative humidity (RH) of 30 %. The sequence starts with a linear rise of the temperature and the relative humidity, from 25°C to 85°C and 30% to 90%, respectively. Next, the temperature is maintained at 85 °C, and the relative humidity varies linearly and cyclically between extreme values. Finally, a hygrothermal unloading is applied by decreasing the temperature and the relative humidity to their initial values.

2.2 Materials model behavior

The material model behavior used in this study is similar to that of Ouerghemmi et al. [43] or Kusoglu et al. [25]. The main equations governing the elasto-plastic model are detailed below.

The components of the total strain tensor, ε_{ij}, are the sum of the elastic strain component, ε_{ij}^{e}, the plastic strain component, ε_{ij}^{pl}, the strain induced by thermal expansion, ε_{ij}^{th}, and the strain induced by swelling, ε_{ij}^{sw}(Eq.1)

$$\varepsilon_{ij} = \varepsilon_{ij}^{e} + \varepsilon_{ij}^{pl} + \varepsilon_{ij}^{th} + \varepsilon_{ij}^{sw} \tag{1}$$

Hook's law is used to describe the evolution of stress, σ_{ij}, as a function of strain in the elastic region for a material with isotropic behavior (Eq.2).

$$\sigma_{ij} = \frac{E}{(1+\nu)(1-2\nu)}\left[\nu\delta_{ij}\varepsilon_{kk}^{e} + (1-2\nu)\varepsilon_{ij}^{e}\right] \tag{2}$$

With σ_{ij}, the components of the stress tensor, ε_{ij}^{e}, the elastic part of the total strain tensor ε_{ij}, E, the Young's Modulus, ν, the Poisson's ratio and δ_{ij} the Kronecker symbol.

For the orthotropic material, the stress/strain relation is given in equation 3 [44]:

$$\begin{pmatrix} \varepsilon_{xx} \\ \varepsilon_{yy} \\ \varepsilon_{zz} \\ 2\varepsilon_{xy} \\ 2\varepsilon_{xz} \\ 2\varepsilon_{yz} \end{pmatrix} = \begin{pmatrix} \frac{1}{E_x} & -\frac{\nu_{yx}}{E_y} & -\frac{\nu_{zx}}{E_z} & 0 & 0 & 0 \\ -\frac{\nu_{xy}}{E_x} & \frac{1}{E_y} & -\frac{\nu_{zy}}{E_z} & 0 & 0 & 0 \\ -\frac{\nu_{xz}}{E_x} & -\frac{\nu_{yz}}{E_y} & \frac{1}{E_z} & 0 & 0 & 0 \\ 0 & 0 & 0 & \frac{1}{G_{xy}} & 0 & 0 \\ 0 & 0 & 0 & 0 & \frac{1}{G_{xz}} & 0 \\ 0 & 0 & 0 & 0 & 0 & \frac{1}{G_{yz}} \end{pmatrix} \begin{pmatrix} \sigma_{xx} \\ \sigma_{yy} \\ \sigma_{zz} \\ \sigma_{xy} \\ \sigma_{xz} \\ \sigma_{yz} \end{pmatrix} \tag{3}$$

Where E_x and E_y are the in-plane Young's moduli, E_z, the out-of-plane Young's modulus, ν_{xy} and ν_{yx} the in-plane Poisson's ratios, $\nu_{zx}, \nu_{zy}, \nu_{xz}$ and ν_{yz} the out-of-plane Poisson's ratios, G_{xy} , the in-plane shear modulus and G_{xz} and G_{yz}, the out-of-plane shear moduli.

When the initial yield limit, σ_{ys_0}, is exceeded, plastic strains occur. The yield function, F_z, defines the limit of the elastic regime (Eq.4).

$$F_z = \phi(\sigma) - \sigma_{ys} \tag{4}$$

Where $\phi(\sigma)$ corresponds to the equivalent stress and σ_{ys} corresponds to the actual yield strength.

Von Mises criterion is used, that corresponds to a critical value of the second deviatoric stress invariant, J_2. This criterion can be written as equation 5:

$$\phi(\sigma) = \sqrt{3J_2 - \sigma_{ys}} \tag{5}$$

With $J_2 = \frac{1}{2}\sigma_{ij}\sigma_{ij} - \frac{1}{6}\sigma_{kk}^2$ and σ_{ij} the components of the Cauchy's stress tensor.

Due to isotropic hardening, yield strength depends on plastic strain. The magnitude of the plastic strain $\overline{\varepsilon^{pl}}$ is defined by the equation 6.

$$\overline{\varepsilon^{pl}} = \int \sqrt{\frac{2}{3} d\varepsilon_{ij}^{pl} d\varepsilon_{ij}^{pl}} \tag{6}$$

With $d\varepsilon_{ij}^{pl}$ the plastic strain increment, equal to equation 7.

$$d\varepsilon_{ij}^{pl} = d\overline{\varepsilon_{ij}^{pl}} \frac{\partial f\left(\sigma_{ij}, \overline{\varepsilon_{ij}^{pl}}\right)}{\partial \sigma_{ij}} = d\overline{\varepsilon_{ij}^{pl}} \frac{3}{2} \frac{S_{ij}}{\sigma_{ys}} \tag{7}$$

With S_{ij} the deviatoric stress tensor.

The materials are subjected to temperature changes during fuel cell operation, which induce thermal expansion. The thermal strain is given by:

$$\varepsilon_{ij}^{th} = \alpha(T - T_0)\delta_{ij} \tag{8}$$

With α the linear coefficient of thermal expansion, T_0 the reference temperature and T the temperature.

In addition, it is commonly accepted that water causes the membrane to swell. The swelling strain of the membrane as a function of temperature, T, and relative humidity, RH, is described by the equation 9.:

$$\varepsilon^s(T, RH) = \sum_{ij}^{4} C_{ij} T^{4-j} H^{4-i} \tag{9}$$

The values of the polynomial constants $C_{ij}$are taken from the literature [25] and given in Table 1.

2.3 Material properties

2.3.1 Bipolar Plates

BPPs are made of 316L stainless steel. The mechanical properties of the BPPs are assumed to follow isotropic linear elastic behavior. Their thermal expansion is neglected in this study.

The mechanical properties of the BPP are summarized in Table 2.

2.3.2 Membrane

The mechanical properties of the membrane (Table 2) are taken from the work of Kusoglu et al. [25] and Tang et al.[45]. They are considered as an elasto-plastic material with isotropic hardening, thermal expansion and swelling. This model has been widely used in the literature ([23,27,43]).

2.3.3 GDL

2.3.3.1 Modeling of the irreversible mechanical behavior under compressive stress

The mechanical behavior of the GDL is set as an elastoplastic orthotropic material with hardening, and the mechanical behavior in compression is adapted from an existing analytical model [34].

This model was chosen because:

- It is easily applicable to all non-woven GDLs;
- It can be modified to fit an elasto-plastic law.

The mechanical behavior of the GDL in compression is divided into 3 parts (Figure 3).

1. Initial mechanical behavior after manufacture: During manufacture, the material endures an initial compression, σ_p, which affect its behavior. This can be described by the equation 10.

$$\sigma_1(\varepsilon) = A_1\left(\left(\frac{\rho_1}{1-\varepsilon}\right)^{n_1} - \rho_1^{n_1}\right) + \sigma_c \quad (10)$$

2. Original mechanical behavior: when the value of σ_p is reached, the GDL recovered its original behavior. This is described by the equation 11.

$$\sigma_2(\varepsilon) = A_2\left(\frac{\rho_1}{1-\varepsilon}\right)^{n_2} \quad (11)$$

3. Mechanical behavior after a compression cycle: The mechanical behavior of the GDL is affected by the previous maximum compression reached, σ_M. This new behavior is described by equation 12.

$$\sigma_3(\varepsilon) = A_3\left(\frac{\rho_1}{1-\varepsilon}\right)^{n_3} \quad (12)$$

with σ_i the mechanical stress, ε the engineering strain, ρ_1 the initial relative density of the GDL, σ_c the contact pressure (equal to 0.1 MPa), n_i dimensionless constants and A_i constants with a dimension of a pressure.

This model requires a set of parameters for each GDL, evaluated in experimental cyclic compression tests. In this study, the parameters needed for the model are given in Table 3.

This model is modified to correspond to an elasto-plastic law with hardening (Eq 13). It allows the prediction of the irreversible strain of the GDL after compression, while maintaining of the orthotropic mechanical behavior.

$$\sigma(\varepsilon) = \sigma_e(\varepsilon) + \sigma_h(\varepsilon) \quad (13)$$

where the subscripts, e, and h, correspond to the elastic and hardening part of the mechanical behavior, respectively.

The principle of the implementation is to define an elastic part that corresponds to the part 3 of the previous model (Figure 3), for a given compression σ_M. Once this stress is exceeded, the model switches to plasticity with strain hardening. The equivalent stress for the GDL corresponds to the compression stress σ_{zz}. The strain-hardening function σ_h is then defined by equations 14:

$$\sigma_h(\varepsilon) = \begin{cases} \sigma_1(\varepsilon) - \sigma_3(\varepsilon_M) \; for \; \varepsilon \leq \varepsilon_p \\ \sigma_2(\varepsilon) - \sigma_3(\varepsilon_M) \; for \; \varepsilon > \varepsilon_p \end{cases} \tag{14}$$

Where ε_M is the strain associated to the maximum compression σ_M and ε_P is the strain corresponding to the stress of the first compression σ_p. The actual maximum strain, ε_M, and the process strain, ε_p, are given in the equations 15 and 16, respectively.

$$\varepsilon_M = 1 - \rho_1 \left(\frac{A_3}{\sigma_m}\right)^{\frac{1}{n_3}} \tag{15}$$

$$\varepsilon_p = 1 - \frac{\rho_1}{\left(\frac{\sigma_p - \sigma_c}{A_1} + \rho_1^{n_1}\right)^{\frac{1}{n_1}}} \tag{16}$$

All the strains are given for an uncompressed GDL, i.e. as received from the supplier. However, the GDLs are already constrained by a previous compression, called σ_{HP}, relative to the MEA hot pressing step, which means that the modelled GDL thickness, $h_{GDL_{HP}}$, is lower than that specified by the manufacturer, h_{GDL_0}:

$$h_{GDL_{HP}} = h_{GDL_0}(1 - \varepsilon_r) \tag{17}$$

With ε_r corresponding to the residual strain after the release of the compression σ_M

$$\varepsilon_r = 1 - \rho_1 \left(\frac{A_3}{\sigma_c}\right)^{\frac{1}{n_3}} \tag{18}$$

The other material properties required for the model are adapted from the work of Ouerghemmi et al. [46] and presented in Table 4.

2.3.3.2 Model validation

To validate the modelling of the GDL, a numerical simulation of a compression test is presented on Figure 4 with the label “Elastoplastic law”. The stress/strain curves are obtained for three successive loading/unloading cycles applied on the GDL at increasing maximum stress values of 2, 4 and 10MPa. The value σ_{HP} of the numerical model is in fact set at 1MPa. These results are compared with those obtained with the analytical law [34] and by an experimental test made with the experimental setup described by Le Carre et al. [31].

It can be noticed that the simulation reproduces accurately the analytical model for the loading part but shows differences for the unloading parts and cannot reproduce the experimental hysteresis pattern during loading/unloading phases. The low mean absolute $\Delta\varepsilon$ = 0.012 and relative $\Delta\varepsilon/\varepsilon$ = 0.052 errors between the experimental data and the elastoplastic model validate the proposed approach. This latter fits well the irreversible strain of the GDL after compression, and differences between the analytical model and the elastoplastic law are mainly occurring around the return to zero stress.

2.3.3.3 Hot pressing process

One way of enhancing interfacial contacts between the different layers of the MEA is the hot pressing process [39,42,47–50]. This specific process is realized prior to the stack clamping. It consists in the application of heat and pressure for a given time duration (typically several minutes) on the MEA components, in order to assemble them. However, a comprehensive comparison of different studies investigating the impact of hot pressing on PEMFCs is inherently challenging. The divergent results can be attributed to the considerable variability of materials, ranges of pressures and temperatures used during the hot pressing process. Various studies employ distinct types of catalysts, ionomers, and support materials, leading to differences in the physicochemical properties of the membrane-electrode assemblies. Moreover, the wide spectrum of pressures and temperatures applied during hot pressing introduces additional complexities, as these parameters significantly influence the morphology and performance of the PEMFC [37,38,51]. The hot pressing process affects the average porosity φ and the thickness of the GDL (Figure 5). The evolution of porosity, φ, as a function of the strain ε is defined by the relation: $\varphi = \frac{\varphi_0 - \varepsilon}{1-\varepsilon}$, with φ_0 corresponding to the initial porosity of the GDL. The original porosity, φ_0.of the GDL SGL22BB is set as 75% [24]. Hot pressing process decreases porosity and thickness (Eq. 17) of the GDL. The Figure 5 shows their variation rate for the different values of σ_{HP}., from 0.5 to 10 MPa, obtained with the analytical model [34]. It appears that the value of σ_{HP} plays a role in the evolution of GDL thickness and porosity. Once the value of σ_P is exceeded, the trend in thickness and porosity variation changes; they tend to increase.

Because of the complex relationships between the changes in GDL thickness, transport properties and electrical resistance, it is not possible to define an optimal target for the pressure applied during hot pressing process without multiphysics simulation. However, the impact of the hot pressing process on the mechanical properties of GDL is obviously important and will be examined in further details in this study.

3. Results and discussions

The initial clamping of the stack followed by a HST (Figure 2) is simulated here for fixed displacement (FD) or fixed pressure (FP). In a first section, the impact of the hygrothermal cycles is studied for a fixed displacement, considering representative values for the hot pressing process parameters and initial clamping pressure of the stack. The second section is dedicated to the analysis of the influence of the type of clamping during hygrothermal cycles. The evolutions of GDL porosity, contact pressure between GDL and BPP, and membrane plasticity are examined. This allows to analyze in details, in the last section, the impact of the hot pressing process on the mechanical behavior of the fuel cell. More precisely, a sensitivity study of the value of σ_{HP} (pressure applied during hot pressing process) is presented and discussed.

3.1 Impact of the hygrothermal loading

In this section, the pressure applied during the hot pressing of the MEA is constant, and set at $\sigma_{HP} = 0.5\ MPa$. To simulate the clamping process, the displacement of the top edge of the upper BPP is blocked after an initial clamping pressure P_m of 1 MPa is reached. These parameters are selected to amplify the effect of the hygrothermal loading on the stresses generated during the swelling of the membrane.

Strong variations of P_m are observed during the HST (Figure 6). The clamping pressure increases by 13% during the first swelling of the membrane, from 1.0 to 1.13 MPa. At the end of the hygrothermal loading, the clamping pressure decreases by 47% compared to its initial value, reaching a value of 0.53 MPa.

Hygrothermal loading also affects the contact pressure P_C between GDL and BPP (Figure 7) which varies along the contact area. As expected, there is a strong difference between the clamping pressure and the contact pressure according to the real contact area between the BPP and the GDL. The reds arrows on Figure 7 represent the intensity of the contact pressure. Contact pressure needs to stay sufficient during hygrothermal cycle to limit the increase of the contact resistance at the interface BPP/GDL [52]. In comparison to the end of the clamping, the contact pressure at the middle of the land during the first swelling increases by 10% to reach 3.06 MPa, and decreases by 50% down to 1.39 MPa at the end of the unloading compared to the end of the clamping process.

These results show that hygrothermal loadings induce irreversible strain on the GDL and the membrane and lead to changes in the contact pressure at the BPP/GDL interfaces. These contact pressure losses increase the electrical contact resistance between GDL and BPP, finally inducing a drop in performance.

The clamping process also affects the average porosity φ of the GDL (Figure 8). During the HST, the porosity varies mainly under the land, because of the blocked displacement imposed on the BPP. Compared to the end of the clamping process, the average porosity under the land decreases during the first swelling by 2%. These variations are small in comparison with those induced by the clamping process, with the average porosity under the land decreasing to 62% at the end of the clamping (As a reminder: $\varphi_0 = 75\%$).

Strong variations of the volumetric plastic strain ($\overline{\varepsilon_{vol}^{pl}} = \varepsilon_{xx}^{pl} + \varepsilon_{yy}^{pl} + \varepsilon_{zz}^{pl}$) of the membrane under the channel are observed during the first cycles, decreasing cycle after cycle. It tends to become constant at the end of the HST (Figure 9.a). During the hydration phase (highest humidity), the volumetric plastic strain increases. Then, during drying phase (temperature remains constant and humidity decreases), the volumetric plastic strain decreases. It should be noticed that it is mainly present under the channel. This behavior is the result of the boundaries conditions of the model. During hygrothermal loading, the membrane cannot deform freely in the in-plane direction, resulting in in-plane stresses varying between tensile and compressive states [25,30]. These variations between tensile and compressive state leads to a reverse yielding, i.e. a decrease of the volumetric plastic strain, accentuated by the change in the yield strength of the membrane due to changes in humidity and temperature. Under the land, the compressive stresses limit the increases of the Von Mises stresses during the swelling of the membrane.

The model can help to understand the evolution of the volumetric plastic strain of the GDL during the clamping process and during the HST. However, the effects of hot pressing process

on the GDL are carried out analytically, and the GDL modelled in the software is set with an initial volumetric plastic strain equal to 0. The volumetric plastic strain plotted on Figure 9.b corresponds to the additional volumetric plastic strain of the GDL under the land occurring during clamping process and the HST. The average volumetric plastic strain of the GDL below the land shows that the clamping process is the main cause of the deformation of the GDL ($\varepsilon_{vol}^{pl} = -20\%$). After the clamping process, the first swelling (cycle = 0.5) of the membrane induces a small additional deformation on the GDL ($\varepsilon_{vol}^{pl} = -22\%$) . Then, the average volumetric plastic strain remains constant during the rest of the HST (Figure 9.b).

Moreover, the clamping process and the HST induce an intrusion of the GDL inside channel, corresponding to the vertical distance between the GDL at the middle of the channel and the land, as described in Figure 7. Figure 10 shows the variation rate of the intrusion of the GDL inside the channel, which increases by 12% during the first swelling of the membrane, and remains at 2% at the end of the hygrothermal loading. This irreversible intrusion is only induced by the irreversible strain of the membrane under the channel during the HST. This intrusion must be limited, as it leads to an increase in gas pressure drops along the channel [53,54].

3.2 Impact of the clamping process (imposed pressure vs imposed displacement):

In this section, the pressure applied during the hot pressing process σ_{HP} remains fixed at 0.5 MPa and both types of clamping are investigated, i.e. fixed pressure (FP) or fixed displacement (FD). The initial clamping pressure P_m is still 1 MPa. The case of fixed displacement is already detailed in the above section. Several parameters are given by the simulation: absolute displacement at the top edge of the anode BPP part (fixed for FD and Figure 11. a for FP), contact pressure between GDL and BPP (Figure 7 for FD and Figure 11.b for FP), intrusion of the GDL (Figure 10 for FD and Figure 11.c for FP), and average volumetric plastic strain of the GDL under the land (Figure 9b for FD and Figure 11.d for FP). It appears that the type of clamping has a strong impact on the GDL and its deformation during the HST.

For FP, the upper BPP endures a displacement during hygrothermal loading to absorb the swelling of the membrane. The Figure 11.a shows the displacement endured by the BPP along the HST. The displacement of the upper BPP decreases by 8% after the first swelling, and increases by 0.4 % at the end of the loading, compared to the end of the clamping process. This new condition indicates that the hygrothermal loading induces a permanent change in the mechanical properties of the components. In the case of a fixed pressure, irreversible strain on the GDL is limited, so these changes are only due to the plasticity of the membrane occurring during the HST.

The contact pressure is nearly unaffected by the hygrothermal loading when the clamping is controlled in pressure (Figure 11.b). FP leads to a more constant contact resistance at the BPP/GDL interfaces and, therefore, to more constant performance.

The variation of the intrusion of the GDL inside the channel during hygrothermal loading is strongly affected by the clamping process (Figure 11.c). The clamping process does influence the middle of the channel: the intrusion, after the initial clamping process, is mainly governed by the swelling and the drying of the membrane during hygrothermal loading. For the FD case, the swelling of the membrane induces an intrusion of the GDL inside the channel, but the land

cannot move. Conversely, the swelling of the membrane induces a displacement of the BPP for the FP case, limiting the intrusion of the membrane inside the channel.

The clamping type affects the average volumetric plastic strain of the GDL under the land (Figure 11.d). For FP, the average volumetric plastic strain does not increase during the swelling of the membrane. This clamping method can limit the irreversible strain caused to the GDL by membrane swelling, and can potentially lead to better performance over time.

These results confirm that a clamping method controlled in pressure limits the irreversible strain on the GDL during fuel cell operation compared to a controlled displacement.

3.3 Impact of the hot pressing process

In this section, the effect of different pressure σ_{HP} applied during hot pressing process is investigated. The values of σ_{HP} varies from 0.5 MPa to 10 MPa to represent a large panel of processes. The FD clamping type is simulated, considering an initial clamping pressure P_m of 1 MPa. These conditions are chosen to intensify the effects of the hot pressing process.

The value of the pressure applied during hot pressing process σ_{HP} has an impact on the evolution of the clamping pressure P_m during the HST (Figure 12.a). The increase of the value of σ_{HP} until 6 MPa leads to a lower decrease of the clamping pressure at the end of the HST (Figure 12.b). The evolution of the variation rate of the clamping pressure follow a linear trend function of σ_{HP}. From $\sigma_{HP} \geq 6\ MPa$, there is no more decrease of the clamping pressure since the GDL no longer endures irreversible strain induced by the HST. In the latter case, the value of σ_{HP} is above the maximal compressive stress occuring in the GDL during the HST.

The hot pressing pressure σ_{HP} also affects the contact pressure between GDL and BPP (Figure 13.a), intrusion (Figure 13.b) and irreversible strain of the GDL (Figure 13.c) during clamping and HST. Similarly to the variation rate of the clamping pressure, the contact pressure and the average volumetric strain of the GDL function of σ_{HP} exhibit two different behaviors before and after $\sigma_{HP} = 6\ MPa$. Before this value, the first swelling of the membrane induces a low increase of the contact pressure at the middle of the land but as well a strong decrease at the end of the HST. At the same time, the average volumetric plastic strain under the land (cf. Figure 1) induced by clamping and HST decreases to reach 0 % for $\sigma_{HP} = 6\ MPa$. For $\sigma_{HP} \geq 6\ MPa$, the first swelling of the membrane induces a strong increase of the contact pressure but it comes back to its initial value at the end of the HST. For the evolution of intrusion function of σ_{HP}, the behavior is also divided in two parts, with a strong decrease of the intrusion before $\sigma_{HP} = 4\ MPa$, and a more steady behavior after this value (Figure 13.c). It can be noticed that even for a high value of σ_{HP}, a permanent change on the intrusion happens: this phenomenon is governed by the volumetric plastic strain of the membrane and not by the irreversible strain of the GDL.

However, a high value of σ_{HP} leads to a poorer initial porosity (Figure 13.d). The porosity is linked with the tortuosity of the GDL [55], and a low porosity of the GDL leads to a low diffusivity of the reactants and to a change in the water management in the fuel cell. The value of the hot pressing process needs to take into account also this change in the porosity of the GDL to optimize the mass transport.

These results provide a better understanding of the impact of hot pressing process on the mechanical properties of the GDL, and of its behavior during lifetime. An optimum value of

σ_{HP} for 6 MPa with a minimal change on the mechanical properties on the GDL during clamping and HST appears, but the multiphysics studies, taking for example into account the decrease in initial diffusivity of the GDL, needs to be integrated to find the best values of σ_{HP} to optimize the performances. Future outlook can help to find an optimal range of hot pressing pressure and avoid the experimental test/error optimization process.

4. Conclusion

The numerical implementation proposed in this study allows an original prediction of the irreversible deformation of the GDL after compression via an elasto-plastic law. 2D numerical simulations investigate the effects of the hygrothermal loading, type of clamping and finally, the hot pressing process.

This model predicts the mechanical behavior of GDL undergoing variations of hygrothermal conditions, and shows the importance of controlling the fuel cell clamping process. The fixed pressure clamping is better in this configuration than the fixed displacement clamping, due to the lower mechanical solicitation imposed to the GDL during HST. This leads to a steadier mechanical behavior of the fuel cell during lifetime, and in fact, to steadier performances.

A study of the impact of the hot pressing process shows that it has a significant impact on the physical properties of GDL. In particular, as the applied pressure during the hot pressing process rises, it induces irreversible strain on the GDL, leading to a decrease in GDL thickness and porosity prior to clamping. Studies of clamping function of σ_{HP} show an optimum value for $\sigma_{HP}$to optimize contact pressure and intrusion while limiting irreversible strain of the GDL.

Further research is needed to find the right balance between these different phenomena and to increase the performance of the fuel cell. The prospect of this study is to implement these results in an electrochemical performance model in order to analyze the effect of the irreversible strain of the GDL caused by the operation of the PEMFC on its performance.

References

1. U. S. D. O. E. State of the States: Fuel Cells in America 2017, (2018).

2. U. S. D. O. E. Fuel Cell Technical Team Roadmap, (2017) https://www.energy.gov/eere/vehicles/articles/us-drive-fuel-cell-technical-team-roadmap.

3. G. Hu et al., *Int. J. Electrochem. Sci.*, 1358–1371 (2019).

4. E. M. Khetabi et al., *Int. J. Hydrog. Energy*, **56**, 1257–1272 (2024).

5. D. Choi, *Int. J. Energy Res.*, **46**, 1168–1179 (2022).

6. Q. Shi, C. Feng, P. Ming, F. Tang, and C. Zhang, *Int. J. Hydrog. Energy*, **47**, 3994–4009 (2022).

7. C.-H. Chien et al., *Energy*, **113**, 1174–1187 (2016).

8. Y. Zhou, G. Lin, A. J. Shih, and S. J. Hu, *J. Fuel Cell Sci. Technol.*, **6**, 041005 (2009).

9. A. M. Dafalla and F. Jiang, *Int. J. Hydrog. Energy*, **43**, 2327–2348 (2018).

10. E. M. Khetabi et al., *J. Power Sources*, **424**, 8–26 (2019).

11. S. Escribano, J.-F. Blachot, J. Ethève, A. Morin, and R. Mosdale, *J. Power Sources*, **156**, 8–13 (2006).

12. P. K. Koorata and S. D. Bhat, *Int. J. Hydrog. Energy*, **46**, 5570–5579 (2021).

13. W. Lee, C.-H. Ho, J. W. Van Zee, and M. Murthy, *J. Power Sources*, **84**, 45–51 (1999).

14. T. J. Mason et al., *J. Power Sources*, **219**, 52–59 (2012).

15. J. Millichamp et al., *J. Power Sources*, **284**, 305–320 (2015).

16. V. Radhakrishnan and P. Haridoss, *Int. J. Hydrog. Energy*, **35**, 11107–11118 (2010).

17. Y. Chen et al., *Membranes*, **12**, 645 (2022).

18. P. Irmscher, D. Qui, H. Janßen, W. Lehnert, and D. Stolten, *Int. J. Hydrog. Energy*, **44**, 23406–23415 (2019).

19. C. Carral and P. Mélé, *Int. J. Hydrog. Energy*, **39**, 4516–4530 (2014).

20. J. de la Cruz, U. Cano, and T. Romero, *J. Power Sources*, **329**, 273–280 (2016).

21. P. A. García-Salaberri, M. Vera, and R. Zaera, *Int. J. Hydrog. Energy*, **36**, 11856–11870 (2011).

22. J. Kleemann, F. Finsterwalder, and W. Tillmetz, *J. Power Sources*, **190**, 92–102 (2009).

23. S. Martemianov, M. Gueguen, J. C. Grandidier, and D. Bograchev, *J. Appl. Fluid Mech.*, **2** (2009) https://www.jafmonline.net/article_1216_fba6d6a2c5ec7c840540f8c49d96ca9c.pdf.

24. L. Shi, S. Xu, and J. Liu, *Int. J. Hydrog. Energy*, **47**, 7902–7914 (2022).

25. A. Kusoglu, A. M. Karlsson, M. H. Santare, S. Cleghorn, and W. B. Johnson, *J. Power Sources*, **170**, 345–358 (2007).

26. Y.-H. Lai, C. K. Mittelsteadt, C. S. Gittleman, and D. A. Dillard, *J. Fuel Cell Sci. Technol.*, **6**, 021002 (2009).

27. W. Liu, D. Qiu, L. Peng, and X. Lai, *Fuel Cells*, **23**, 170–180 (2023).

28. M. N. Silberstein and M. C. Boyce, *J. Power Sources*, **196**, 3452–3460 (2011).

29. Y. Tang, M. H. Santare, A. M. Karlsson, S. Cleghorn, and W. B. Johnson, *J. Fuel Cell Sci. Technol.*, **3**, 119–124 (2006).

30. M. Ouerghemmi, C. Carral, and P. Mele, V. Cigolotti, Editor. *E3S Web Conf.*, **334**, 04020 (2022).

31. T. Le Carre, J.-F. Blachot, J.-P. Poirot-Crouvezier, and J. Laurencin, *Int. J. Hydrog. Energy*, S0360319923040855 (2023).

32. M. A. R. S. Al-Baghdadi, *Int. J. Energy Environ.*, **7**, 26 (2016).

33. P. K. Koorata, *J. Electrochem. Soc.*, **169**, 104505 (2022).

34. C. Carral and P. Mele, *Int. J. Hydrog. Energy*, **47**, 23348–23359 (2022).

35. C. Carral and P. Mélé, *Int. J. Hydrog. Energy*, **43**, 19721–19729 (2018).

36. V. Norouzifard and M. Bahrami, *J. Power Sources*, **264**, 92–99 (2014).

37. J. Hack et al., *J. Electrochem. Soc.*, **165**, F3045–F3052 (2018).

38. D. Ramani et al., *J. Power Sources*, **512**, 230431 (2021).

39. Z. Shangguan, B. Li, P. Ming, and C. Zhang, *J. Mater. Chem. A*, **9**, 15111–15139 (2021).

40. J. Hinebaugh, J. Lee, and A. Bazylak, *J. Electrochem. Soc.*, **159**, F826–F830 (2012).

41. P. K. Koorata and S. D. Bhat, *Int. J. Hydrog. Energy*, **47**, 1217–1228 (2022).

42. M. Ouerghemmi et al., *Int. J. Hydrog. Energy*, S0360319923041915 (2023).

43. M. Ouerghemmi, thesis, (2022).

44. A. P. Boresi, R. J. Schmidt, and O. M. Sidebottom, *Advanced mechanics of materials*, 5. ed., p. 811, Wiley, New York, (1993).

45. Y. Tang et al., *Mater. Sci. Eng. A*, **425**, 297–304 (2006).

46. M. Ouerghemmi, C. Carral, and P. Mele, *J. Electrochem. Soc.*, **170**, 104508 (2023).

47. S. M. Andersen, R. Dhiman, M. J. Larsen, and E. Skou, *Appl. Catal. B Environ.*, **172–173**, 82–90 (2015).

48. I. Gatto et al., *J. Energy Chem.*, **35**, 168–173 (2019).

49. M. Najafi Roudbari, R. Ojani, and J. B. Raoof, *Energy*, **140**, 794–803 (2017).

50. A. Therdthianwong, P. Manomayidthikarn, and S. Therdthianwong, *Energy*, **32**, 2401–2411 (2007).

51. S. Shahgaldi, I. Alaefour, and X. Li, *Appl. Energy*, **225**, 1022–1032 (2018).

52. L. Zhang et al., *J. Power Sources*, **162**, 1165–1171 (2006).

53. S. G. Kandlikar, Z. Lu, T. Y. Lin, D. Cooke, and M. Daino, *J. Power Sources*, **194**, 328–337 (2009).

54. Y.-H. Lai, P. A. Rapaport, C. Ji, and V. Kumar, *J. Power Sources*, **184**, 120–128 (2008).

55. L. Holzer et al., *Tortuosity and Microstructure Effects in Porous Media: Classical Theories, Empirical Data and Modern Methods*, Springer International Publishing, Cham, (2023) https://link.springer.com/10.1007/978-3-031-30477-4.

Glossary

$PEMFC$	Proton Exchange Membrane Fuel Cells
GDL	Gas Diffusion Layer
FEM	Finite Element Model
MEA	Membrane Electrode Assembly
CCM	Catalyst Coated Membrane
BPP	BiPolar Plate
FD	Fixed Displacement (Clamping)
FP	Fixed Pressure (Clamping)
HST	Hygrothermal Stress Test
RH	Relative Humidity
T	Temperature

Symbols

ε	Total strain tensor
σ	Stress tensor
δ_{ij}	Kronecker symbol
E	Young Modulus
ν	Poisson's ratio
G	Shear modulus
σ_{ys_0}	Initial yield limit
ϕ	Equivalent stress
σ_{ys}	Actual yield limit
J_2	Second deviatoric stress invariant
S	Deviatoric stress tensor
T_0	Reference temperature
α	Linear coefficient of thermal expansion
$\sigma_1, \sigma_2, \sigma_3$	Part of the analytical model
h_{GDL}	Thickness of the GDL
P_m	Clamping pressure
P_c	Contact pressure
φ	Porosity
σ_p	Pressure applied during GDL manufacturing process

Subscripts and superscripts

ij	Tensor's Component
e	Elastic
pl	Plastic
th	Thermal
sw	Swelling
x, y, z	x, y, z directions
xy, yx	xy, yx plane, in-plane
xz, zx, yz, zy	xz, zx, yz, zy plane, out-of-plane
h	Hardening part
M	Maximum compression
HP	After Hot Pressing process
0	Initial state
r	Residual strain
vol	Volumetric

Figures

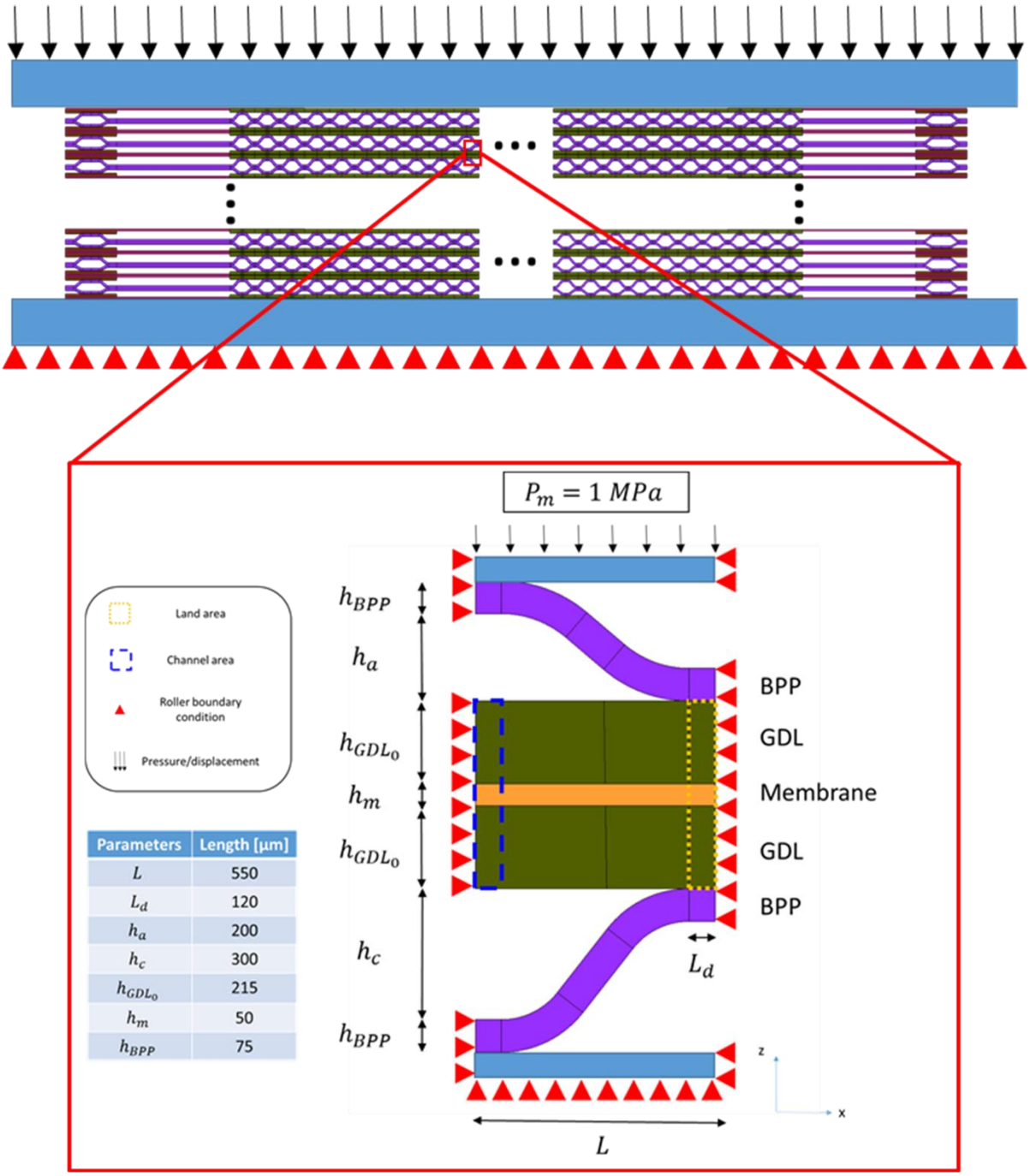

Parameters	Length [µm]
L	550
L_d	120
h_a	200
h_c	300
h_{GDL_0}	215
h_m	50
h_{BPP}	75

Figure 1: Geometry and boundaries conditions of a 2D representative element of a fuel cell.

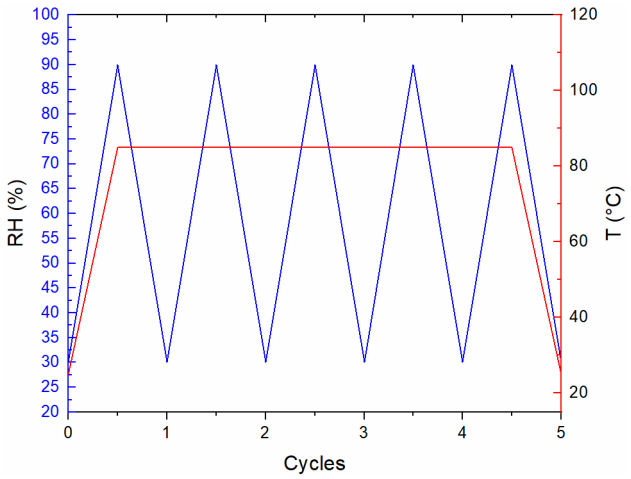

Figure 2: Hygrothermal loading sequence defining the Hygrothermal Stress Test (HST) adapted from [25]

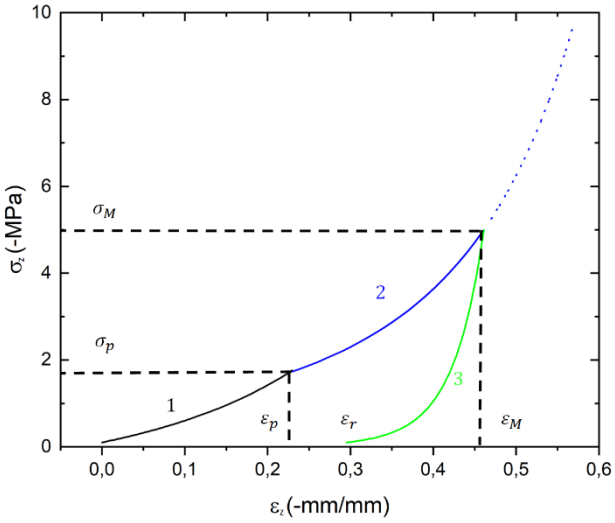

Figure 3: Diagrams of the 3 parts of the model, adapted from [34]

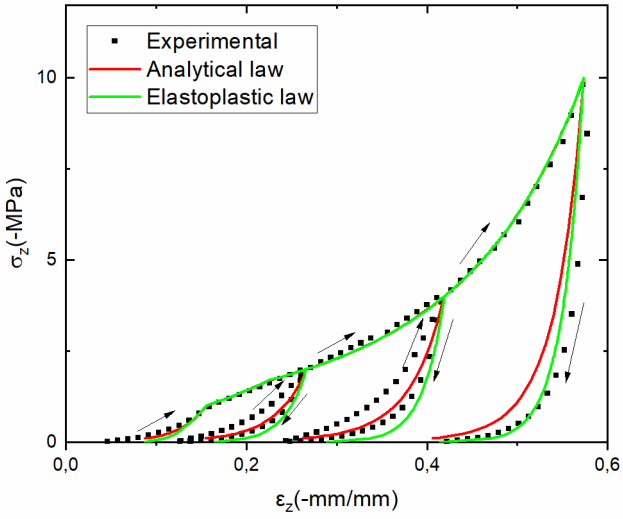

Figure 4: Comparison of the experimental stress/strain curves with those obtained using EF simulation (Elastoplastic law), the analytical model [34] and experimental measurements

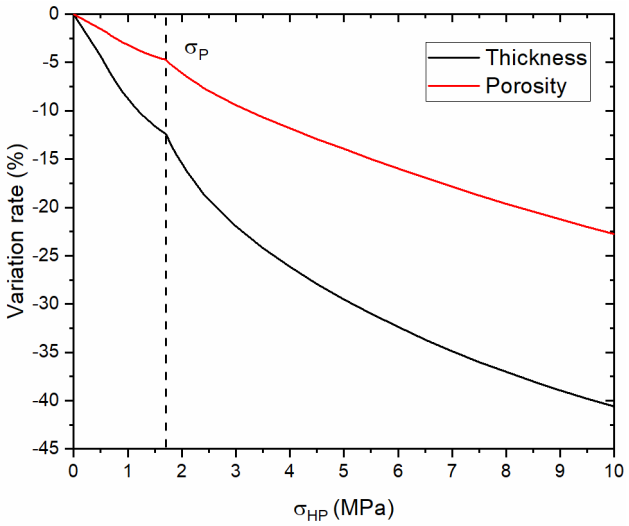

Figure 5 : Evolution of GDL porosity and GDL thickness after hot pressing process as function of σ_{HP}. The value corresponding to the initial compression σ_P endures by the GDL during the manufacturing process is highlighted by a dashed line.

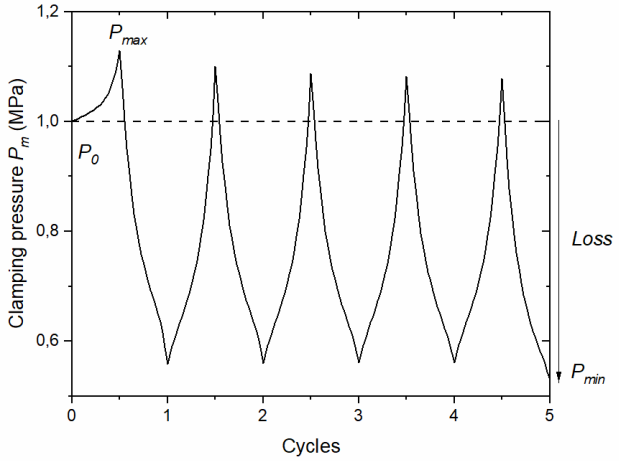

Figure 6: Evolution of the clamping pressure during hygrothermal cycles ($\sigma_{HP} = 0.5\ MPa$, FD)

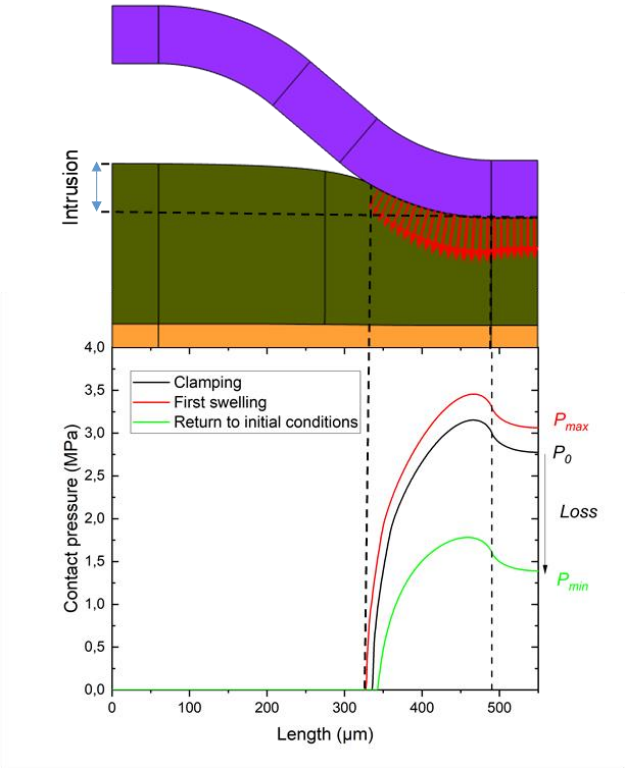

Figure 7: Evolution of contact pressure during hygrothermal loading ($\sigma_{HP} = 0.5\ MPa$, FD)

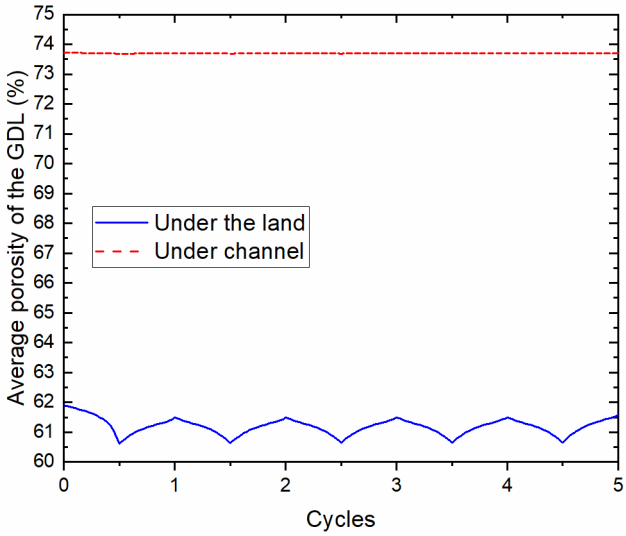

Figure 8: Variations of the porosity during hygrothermal cycles ($\sigma_{HP} = 0.5\ MPa$, FD)

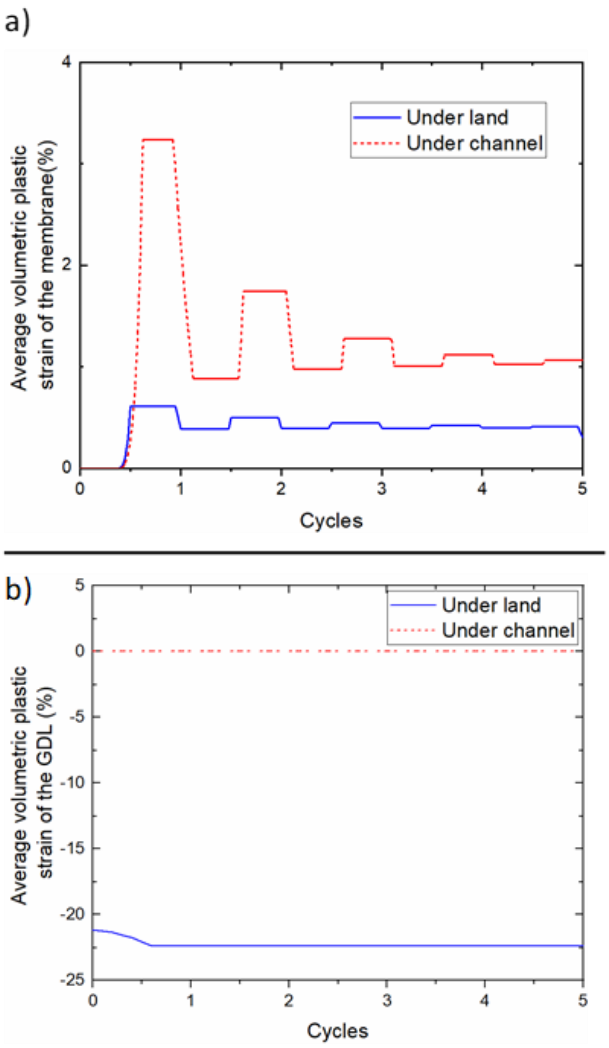

Figure 9: Evolution of average volumetric plastic strain of a) the membrane and b) the GDL during hygrothermal loading ($\sigma_{HP} = 0.5\ MPa$, FD)

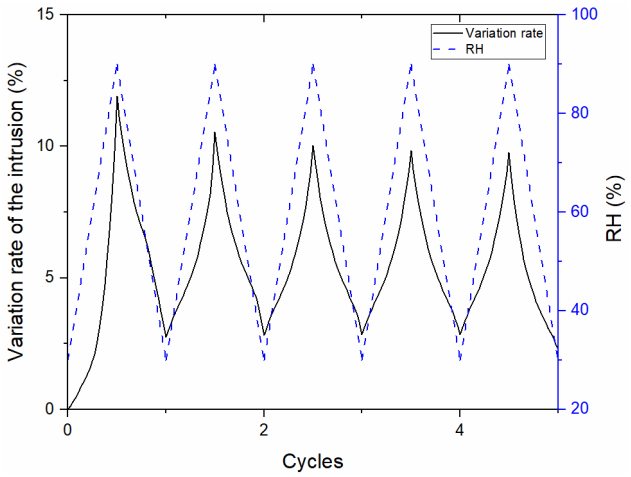

Figure 10: Evolution of the intrusion of the GDL inside channel during hygrothermal loading, anode side ($\sigma_{HP} = 0.5\ MPa$, FD)

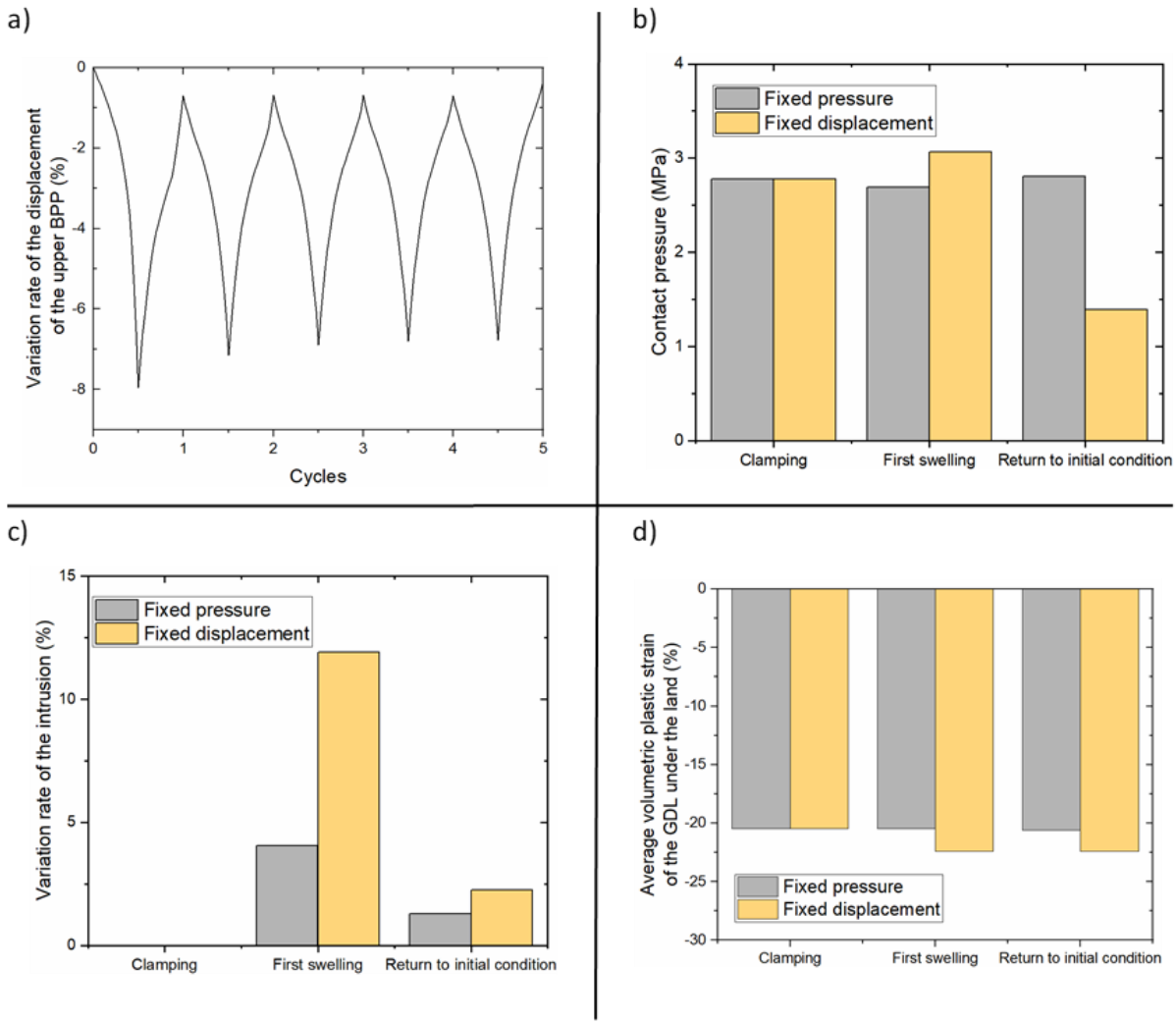

Figure 11: a) Evolution of the displacement of the upper BPP b) Contact pressure at the interface BPP/GDL at the middle of the land c) Intrusion of the GDL at the middle of the channel d) Average volumetric plastic strain of the GDL under the land ($\sigma_{HP} = 0.5\ MPa$)

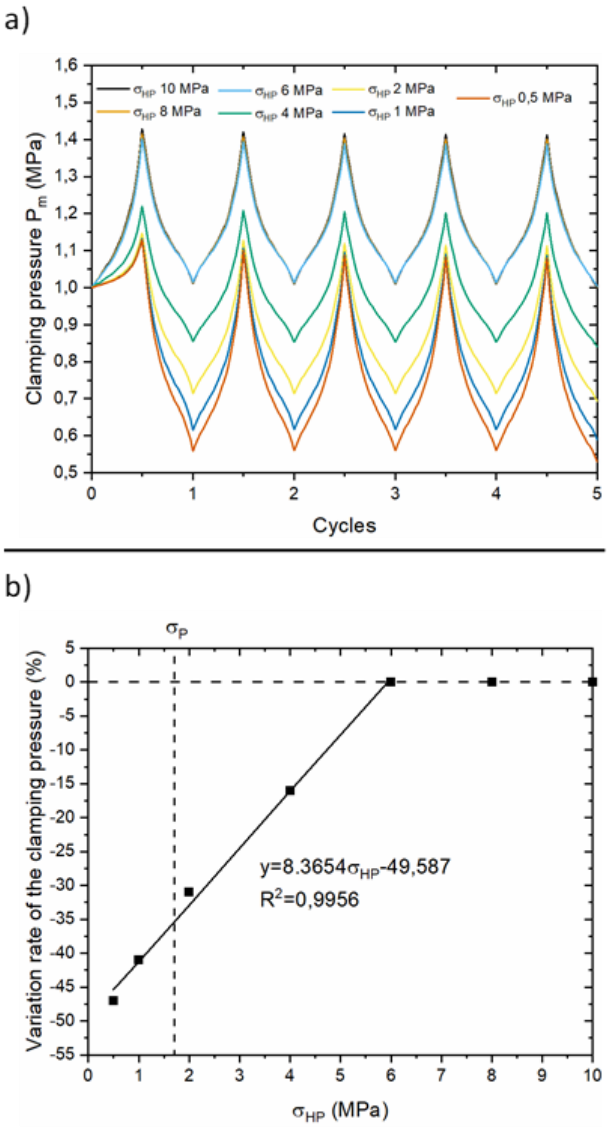

Figure 12: a) Evolution of the clamping pressure P_m during hygrothermal loading for different values of σ_{HP} b) Variation rate of the clamping pressure at the end of the HST for the different values of σ_{HP}. (FD)

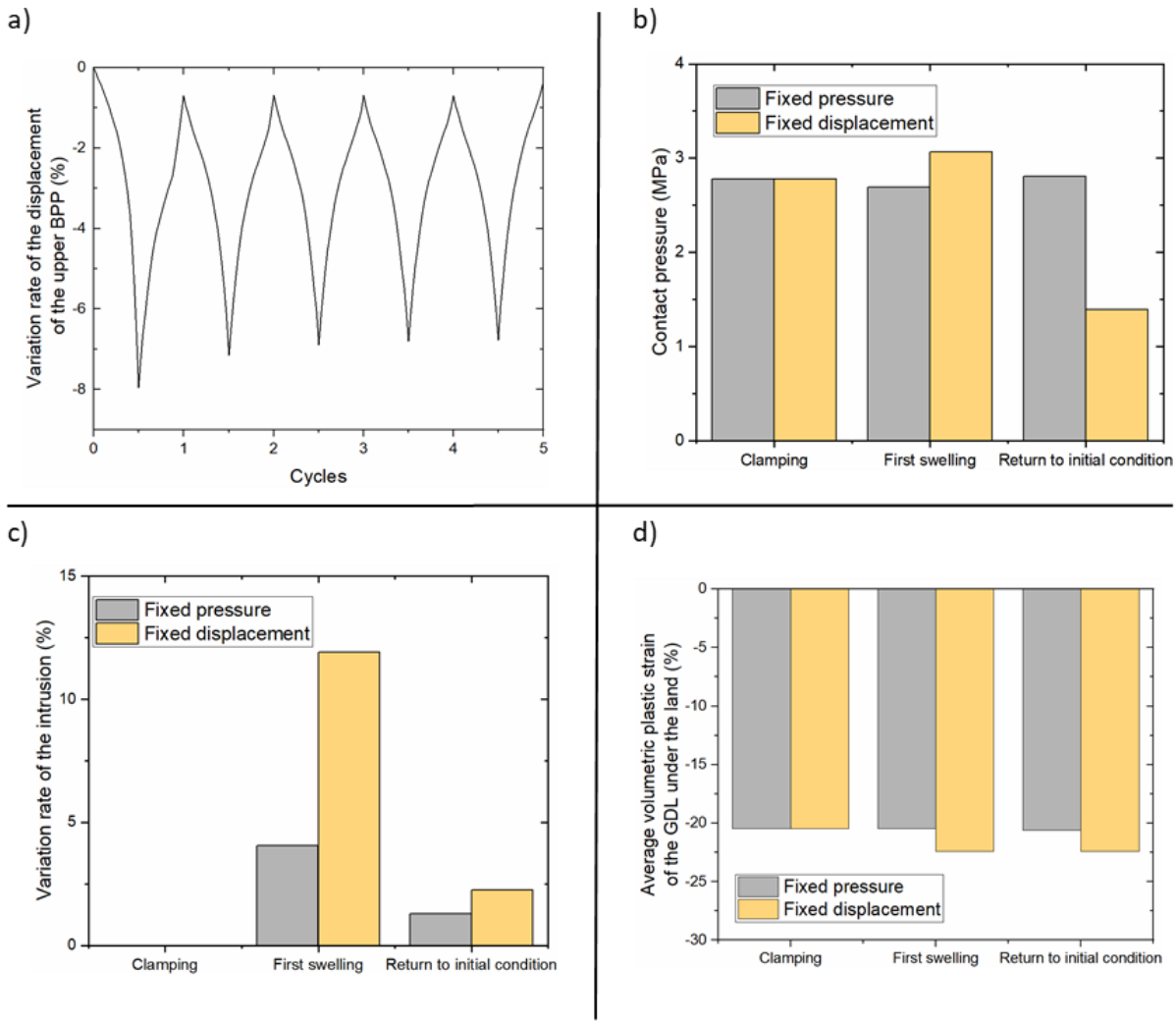

Figure 13: Values of the a) contact pressure between BPP/GDL at the middle of the land b) the variation of the intrusion of the GDL at the middle of the channel c) the added volumetric plastic strain for different value of σ_{HP} at the end of the clamping process and d) the average porosity of the GDL under the land (cf Figure 1), after the end of the clamping process, the first swelling of the membrane and at the return to the initial conditions. (FD)

Tables

C_{ij}	$i=1$	$i=2$	$i=3$	$i=4$
$j=1$	2.994×10^{-12}	-5.221×10^{-10}	3.574×10^{-8}	-6.832×10^{-7}
$j=2$	-4.303×10^{-10}	7.361×10^{-8}	-5.166×10^{-6}	1.003×10^{-4}
$j=3$	2.163×10^{-8}	-3.566×10^{-6}	2.564×10^{-4}	-5.067×10^{-3}
$j=4$	-5.402×10^{-8}	2.012×10^{-5}	2.007×10^{-3}	4.355×10^{-2}

Table 1: Values of the constants C_{ij} according to [25]

Component	Material	E	ν	α	Thickness
Foil of BPP	Stainless steel 316l	205 $[GPa]$	0.3	$16.5\times10^{-6}\ [K^{-1}]$	75 [μm]
Membrane	Nafion 112	$f(T,RH)$ [25]	0.25	$123e-6\ [K-1]$ [25,45]	50 [μm]

Table 2: Physical properties of the BPP and the membrane

Ref.	σ_p [MPa]	ρ_1	A_1 [MPa]	n_1	n_2	B	C [MPa]	n_{3_0}
22BB	1.7	0.194	281.6	3.33	2.97	35.5	1.26	13.9

Table 3: Parameters of the model for the compression of the GDL (Sigracet SGL22B)

Parameter	Unit	Value
E_x	MPa	2700
E_y	MPa	1900
ν_{xz},ν_{yz}	-	0
ν_{xy}	-	0.2
G_{xz},G_{yz}	MPa	2.4
G_{xy}	MPa	193
h_{GDL_0}	µm	215

Table 4: Material model parameters – GDL (Sigracet SGL 22BB)